Highly efficient multi-metal catalysts for carbon dioxide reduction prepared from atomically sequenced metal organic frameworks

Celia Castillo-Blas[1,†], Consuelo Álvarez-Galván[2] (✉), Inés Puente-Orench[3,4], Alba García-Sánchez[5], Freddy E. Oropeza[5], Enrique Gutiérrez-Puebla[1], Ángeles Monge[1] (✉), Víctor A. de la Peña-O'Shea[5] (✉), and Felipe Gándara[1] (✉)

[1] *Materials Science Institute of Madrid (CSIC), C/Sor Juana Inés de la Cruz 3, Madrid 28049, Spain*
[2] *Instituto de Catálisis y Petroleoquímica (CSIC), C/Marie Curie 2, Madrid 28049, Spain*
[3] *Instituto de Ciencia de Materiales de Aragón, Pedro Cerbuna 12, Zaragoza 50009, Spain*
[4] *Institut Laue Langevin, 71 Avenue des Martyrs, 38042 Grenoble, France*
[5] *Photoactivated Processes Unit IMDEA Energy Institute, Móstoles Technology Park, Avenida Ramón de la Sagra 3, Móstoles, Madrid 28935, Spain*
[†] *Present address: Department of Inorganic Chemistry, University Autonomous of Madrid, C/Francisco Tomás y Valiente 7, Madrid 28049, Spain*

1 Introduction.

Reducing the global temperature raise to mitigate the associated climate change has already become an emergency issue for our society. The continuous raise of global energy demand, which is largely fulfilled with the combustion of fossil fuels, results in the unceasing increase of the amount of greenhouse effect gases that are emitted to the atmosphere. While we transition towards a zero-emission economy based on clean and renewable energy sources it is crucial to mitigate this amount of emitted gas [1].

Considering that carbon dioxide is the main greenhouse gas, the reutilization of this molecule to be converted in other added-value products is one of the actions to be taken during this transition. In this regard, there are a few chemical processes where carbon dioxide is valorized to synthesize urea, salicylic acid, or polycarbonates. Another interesting route to recycle carbon dioxide is the production of sustainable fuels through its reduction to carbon monoxide, which can be further employed as chemical building block in the Fischer-Tropsch and/or methanol synthesis to produce hydrocarbons or oxygenates [2]. In this sense, reverse water-gas shift (RWGS) is still one of the most important industrial reactions for this purpose. Through the RWGS reaction, CO_2 is reduced to carbon monoxide by hydrogen gas. RWGS is an endothermic reaction, which is favored at high temperature (~ 700–800 °C). A number of catalytic systems have been investigated for this reaction [3], including perovskite type oxides as catalytic precursors [4], copper nanoparticles [5], and others [6]. Among them, catalysts based on metal nanoparticles supported on reducible oxides have shown very promising activity [7], with a strong influence of the preparation procedure on the obtained activity and selectivity, as consequence of the interplay between compositional, structural, and morphological features of the system. Therefore, the development of routes for the obtaining of supported metal nanoparticles with high metal–support interface and accessible surface is greatly desirable.

Metal-organic frameworks (MOFs) are a class of reticular materials, formed by the joining of metal clusters through organic linkers, to produce robust, extended networks with desired topological and geometrical features [8]. Due to their porous nature, MOFs have been extensively studied for applications related to carbon dioxide capture [9, 10], and they are currently being investigated for a number of processes related to carbon dioxide transformations, such as electro- or photoreduction [11], as well as chemical fixation to other molecules [12].

In addition to direct use of MOFs as catalyst, their transformation into other solids [13] has been shown to be a suitable way to produce new catalytically active materials for a range of different reactions [14, 15]. This is particularly useful in the cases where the required reaction conditions are not compatible with the direct use of MOF samples, such as high temperature. The main advantage of using MOFs to create other solids relies on the possibility of translating some of the MOF features to the products resulting from the transformation reaction. For example, carbonaceous materials with desired metal nanoparticles have been obtained by MOFs pyrolysis through different routes [16]. The high crystallinity of MOFs, along with the unpaired degree of control on the disposition of their components, provides a unique platform to assembly desired metal elements in specific chemical environments, which can be maintained during the subsequent transformation. Through this way, it is possible to modify and control the structural and compositional features of the products resulting from the MOF transformation, in a way that is not possible with conventional synthetic routes.

Recently, we demonstrated that various metal elements can be combined and form different arrangements and elemental sequences in the secondary building unit (SBU) of a metal-organic framework [17]. The choice of the initial metal combinations and molar ratios determines the resulting type of distribution and elemental sequence. Moreover, this resultant distribution of metal elements in the SBUs has a direct impact on the structure and composition of the solid that is obtained upon calcination of the MOF. In particular, we found that oxides with spinel type structure can be obtained from calcination of MOFs with a range of compositions including combinations of three or four different elements, namely zinc, cobalt, manganese, and calcium. Most importantly, the metal-ratio of the resulting spinel oxides are directly translated from the MOF precursor, and could be adjusted to enhance the electrocatalytic activity of these solids in the reduction of oxygen [18]. Following, in the present study we show that spinel oxides obtained from the MOF calcination route can be used as precursor catalyst for the reverse water-gas shift reaction. Under the RWGS reaction conditions, with reducing atmosphere and high temperature, the spinel oxides are *in-situ* transformed to the catalytically active species, consisting of manganese-calcium oxide supported cobalt nanoparticles (Scheme 1). The spinel composition and structure, which are pre-programmed from the metal arrangements in the SBUs of the parent MOF, determine the activity

and selectivity of the obtained catalytic system through differences in their reduction process. The structure of the obtained spinel oxides has been investigated with neutron powder diffraction measurements, and the resulting catalysts have been characterized with combination of electron microscopy and spectroscopic analyses, as well as temperature programmed reduction, and *in situ* X-ray photoelectron spectroscopy (XPS). The results of this study illustrate the advantage of using reticular chemistry to program desired compositions in oxides, which ultimately determine their activity under required catalytic reaction conditions.

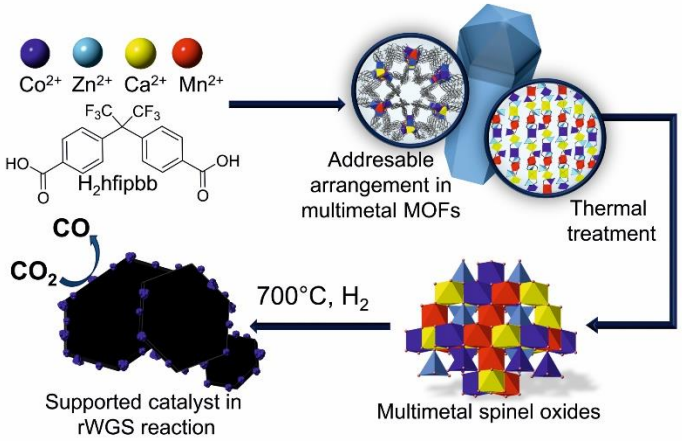

Scheme 1 Multimetal MOFs are formed by the combination of selected cations (Zn^{2+}, Co^{2+}, Mn^{2+} and Ca^{2+}) with an organic linker (H_2hfipbb). After thermal treatment of this multimetal MOFs, multication spinel oxides maintaining compositions are obtained. Under RWGS reaction conditions, the spinel oxides are *in-situ* transformed to catalytic active species, consisting of oxide supported nanoparticles.

2 Experimental

2.1 MOF synthesis

MOFs with selected metal combinations were prepared according to reported procedures [18]. The general MOF preparation consists of mixing the organic linker 4,4,'-(hexaflouroisopropylidene)bis(benzoic acid) ($C_{17}H_{10}O_4F_6$, H_2hfipbb) and the corresponding metal salts in a water/ethanol/nitric acid solution, followed by heating at 170 °C overnight. An example of the synthetic method is given for the MOF with formula $Zn_{0.17}Mn_{0.47}Co_{0.33}Ca_{0.03}$(hfipbb): H_2hfipbb (78 mg 0.2 mmol), $Zn(NO_3)_2{\cdot}6H_2O$ (10 mg, 0.033 mmol), $MnCl_2{\cdot}6H_2O$ (26 mg, 0.132 mmol), $Co(NO_3)_2{\cdot}6H_2O$ (38 mg, 0.132 mmol) and $Ca(NO_3)_2{\cdot}6H_2O$ (8 mg, 0.033 mmol) were dissolved in 10 mL of a 1:1 water:ethanol mixture, and 300 µL of a 1 M HNO_3 aqueous solution were subsequently added. The mixture was stirred at room temperature for 5 min, placed in a Teflon-lined steel autoclave and heated at 170 °C overnight. After cooling to room temperature in air, blue needle-shaped crystals were filtered off, washed with 20 mL of water and acetone and dried under dynamic vacuum. All the other MOFs were similarly prepared employing the required amounts of the metal salts.

2.2 Spinel preparation

Spinel oxides were obtained according to the procedure reported in Ref. [18]. In short, the selected MOF was placed in a zirconia crucible, and heated in a furnace from room temperature to 800 °C with a heating rate of 5 °C·min^{-1}. The samples were kept at 800 °C for 24 h, and then cooled down to room temperature.

2.3 Catalytic experiments

The catalytic behavior of the catalysts for the RWGS reaction was studied under atmospheric pressure, at 700 °C using a quartz fixed bed reactor (external diameter = 6 mm, internal diameter = 4 mm). The temperature was increased under the reaction feed (30 cm^3·min^{-1} of H_2, 15 cm^3·min^{-1} of CO_2 and 5 cm^3·min^{-1} of N_2) up to the reaction temperature (700 °C) with a ramp of 15 °C·min^{-1}. The space velocity was 300,000 mL·h^{-1}·g^{-1}. The reaction stream was analyzed on line by gas chromatography (HP 6890), with a chromatograph equipped with a column Carboxen 1010 PLOT (SUPELCO®) and a thermal conductivity detector. This system was used to analyze H_2, O_2, N_2, CO, CO_2 and CH_4. Nitrogen was selected as an inert standard for quantification.

2.4 Temperature programmed reduction (TPR) study

TPR studies have been conducted on a TPD/R/O 1100 instrument (CE Instruments). TPR studies were carried out by passing 5 vol.% H_2 (Ar) at a flow of 100 mL·min^{-1} over the catalyst sample. The temperature was increased to 900 °C with a heating ramp of 10 K·min^{-1}.

2.5 Transmission electron microscopy (TEM)-energy dispersive X-ray spectroscopy (EDS)

Selected area electron diffraction (SAED) and TEM images were achieved with an JEOL JEM 2100 transmission electron microscope operated at an accelerating voltage of 200 kV, equipped with an ESED and an INCAx-sight detectors of Oxford Instruments. Images were processed using Gatan Digital micrograph [19] and Image J [20] softwares.

2.6 Powder X-ray diffraction (PXRD)

PXRD patterns were measured using a Bruker D8 diffractometer with a copper source operated at 1,600 W, covering a 2θ range of 2.5° to 80° with step size = 0.02° and exposure time = 0.5 s per step. PXRD measurements were used to check the purity of the obtained microcrystalline products by comparison of the experimental results with the reported calculated patterns [21, 22].

2.7 Neutron powder diffraction (NPD)

NPD experiments were performed on the high resolution instrument D2B at the Institut Laue-Langevin in Grenoble (France). The samples were contained in a 6-mm cylindrical vanadium holder. The data sets were collected with calibrated neutrons of wavelength 1.594743 Å, covering a 2θ range of 0.2° to 150°, every 0.05° at room temperature. The data reduction (including the application of some basic operations as those related with the addition of several patterns or detector efficiency corrections) was carried out with the LAMP software [23]. Rietveld refinements were performed using the Reflex module of Materials Studio 8.0 [24].

Table 1 Detailed formulae and catalyst number of studied materials

Catalyst	MOF code[a]	MOF formula[b]	Spinel formula[c]	NPD refinement site assignment $(A)(B)_2O_4$[d]
#1	ZnMnCoCa 1441	$Zn_{0.17}Mn_{0.47}Co_{0.33}Ca_{0.03}$(hfipbb)	$Zn_{0.51}Mn_{1.41}Co_{0.99}Ca_{0.09}O_4$	$(Zn_{0.54}Co_{0.46})(Mn_{1.4}Co_{0.51}Ca_{0.09})O_4$
#2	MnCoCa 122	$Mn_{0.23}Co_{0.50}Ca_{0.27}$(hfipbb)	$Mn_{0.69}Co_{1.50}Ca_{0.81}O_4$	$(Co_1)(Mn_{0.7}Co_{0.5}Ca_{0.8})O_4$
#3	ZnMnCoCa 1111	$Zn_{0.41}Mn_{0.41}Co_{0.10}Ca_{0.08}$(hfipb	$Zn_{1.23}Mn_{1.23}Co_{0.30}Ca_{0.24}O_4$	$(Zn_1)(Zn_{0.26}Mn_{1.24}Co_{0.34}Ca_{0.18})O_4$

		b)		
#4	ZnMnCo 118	$Zn_{0.22}Mn_{0.32}Co_{0.46}$(hfipbb)	$Zn_{0.66}Mn_{0.96}Co_{1.38}O_4$	$(Zn_{0.68}Co_{0.32})(Mn_{0.9}Co_{1.1})O_4$

[a]Code indicates the initial metal molar ratio selected for MOF preparation. [b,c]Determined with ICP analysis. [d]Occupancies and positions determined with NPD Rietveld refinement.

2.8 X-ray powder thermodiffraction (XRPTD)

Powder X-ray diffractograms were collected *in situ* with variable temperature to determine the phase change with the temperature and under reducing atmosphere. The thermodiffractograms were collected using a Bruker diffractometer using Cu Kα radiation (λ = 1.54178 Å) at a scanning rate of 0.03 °/s in the 2θ range 25° to 70° . The experiment was performed with a heating ramp of 5 °C/min from 30 to 700 °C in a mixture of 2:1 of H_2/CO_2, and the diffractograms were recorded every 25 °C.

2.9 Near-ambient pressure X-ray photoelectron spectroscopy (NAP-XPS)

Spectra were recorded on a lab-based spectrometer (SPECS GmbH, Berlin) using a monochromated AlKα_1 source ($h\nu$ = 1486.6 eV) operating at 50 W. The X-rays are microfocused to give a spot size on the thin films of 300 µm in diameter. The analyser is a SPECS PHOIBOS 150 NAP, a 180° hemispherical energy analyser with 150 mm mean radius. The entrance to the analyser is a nozzle with a 300 µm diameter orifice. The total energy resolution of the measurements was about 0.50 eV. The BE was calibrated against the Au Fermi level. Samples were exposed to a 2 mbar total pressure of a 2:1 H_2:CO_2 reactive mixture and the temperature was increased from room temperature to 600 °C .

3 Results and discussion

3.1 Neutron powder diffraction study of MOF derived multi-metal spinel oxides.

In our recent work, we showed that multi-metal spinel type oxides can be obtained from MOF calcination, and that the composition of the oxides is translated from the MOF. Indeed, the initial arrangement of metal elements in the MOF SBU is a key factor directing the obtaining of pure-phase spinel oxides or a mixture of different products. Thus, we found that bimetallic MOF precursors resulted in a mixture of different oxides, while in the case of MOFs composed of three and four metal elements, it was possible to obtain spinel oxides with a wide range of different compositions. We have now completed a neutron powder diffraction study on the obtained spinel oxides with selected compositions, as detailed in Table 1, to further confirm the presence and location of the different cations in the spinel structure. Results of the Rietveld refinements (Fig. 1) confirm phase purity, and that in all cases the spinel oxides exhibit a cubic structure, with space group $Fd\bar{3}m$. According to the generic AB_2O_4 spinel formula, A is a divalent cation in tetrahedral coordination, and B is a trivalent cation in octahedral environment. Other cationic organization in spinel structures comprise presence of trivalent cations in tetrahedral sites and divalent cations in octahedral environment, such as $(A_{1-x}B_x)[A_xB_{1-x}B_1]O_4$, or $(B_{1-x}A_x)[A_{1-x}B_{1+x}]O_4$, resulting in different inversion degrees (λ). Assignment of the metal sites was thus conducted with Rietveld refinement of the neutron diffraction patterns. Accordingly, in all cases we found that zinc atoms are occupying the tetrahedral sites in the spinel structure. They are only found with octahedral environment in the spinel sample #3, with a larger amount of this element in the formula. Conversely, when the amount of zinc is smaller, the occupation of the tetrahedral sites is completed with cobalt atoms. For sample #2, which is the only one prepared with absence of zinc, all tetrahedral sites are occupied by cobalt atoms, and according to the NPD refinements, manganese atoms are exclusively located in the octahedral B sites. When calcium atoms are present in the spinel, they must be in octahedral sites (inducing an inversion of the structure with divalent cations in the B positions). Thus, in samples #1 and #2, trivalent cobalt atoms are in the tetrahedral A positions compensating charge. However, in the zinc rich sample #3, divalent calcium and zinc atoms are occupying B sites. Since all tetrahedral A sites are filled with divalent zinc atoms, charge must be balanced with presence of octahedral manganese(IV) cations.

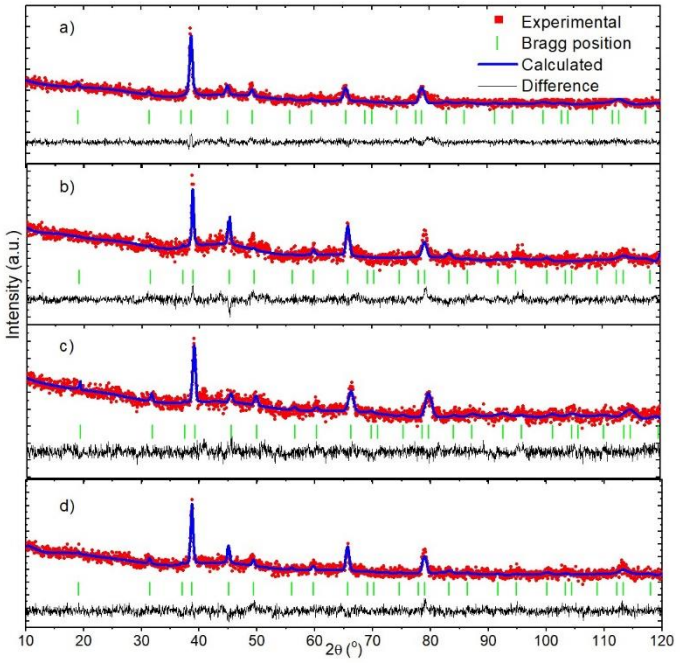

Figure 1 Rietveld refinement of neutron powder diffraction patterns for spinel oxides #1 to #4 (a)–(d).

3.2 Reduction studies

Considering that RWGS process is mainly favored by supported metallic nanoparticles and that this reaction is conducted under reductive atmosphere, we conducted a TPR study for the MOF-derived spinel oxides to get further insight about the effect of H_2 in the reduction process and its relationship with catalytic phases evolution during activation and reaction. Figure 2 shows the TPR curves obtained for all the materials. Samples #1, #2 and #4 show a first reduction stage with a maximum around 375 °C, which is at 450 °C for sample #3. According to literature, this is attributed to the reduction of Co(III) to Co(II) cations which is consistent with mixed metal spinel oxides, where this reduction is exhibited at higher temperature than in single metal spinel oxides, where an intermediate solid-solution oxide is formed [25]. Mn(III) to Mn(II) reduction cannot be ruled out to be contributing to this signal and *in situ* experiments are necessary to shed light to the contribution of this peak. The second reduction stage starts between 450 and 600 °C

with a maximum around 640 °C for #1, #2 and #4. These features are mainly attributed to the cobalt reduction from Co(II) to metallic cobalt and the reduction of remaining Mn(III) to Mn(II) that might form mixed oxides with Ca(II), that is more difficult to be reduced. In the case of sample #3 these reductions steps start at 600 °C with a maximum at 700 °C, indicating that the increase in Zn concentration leads to an increase in the reduction temperature.

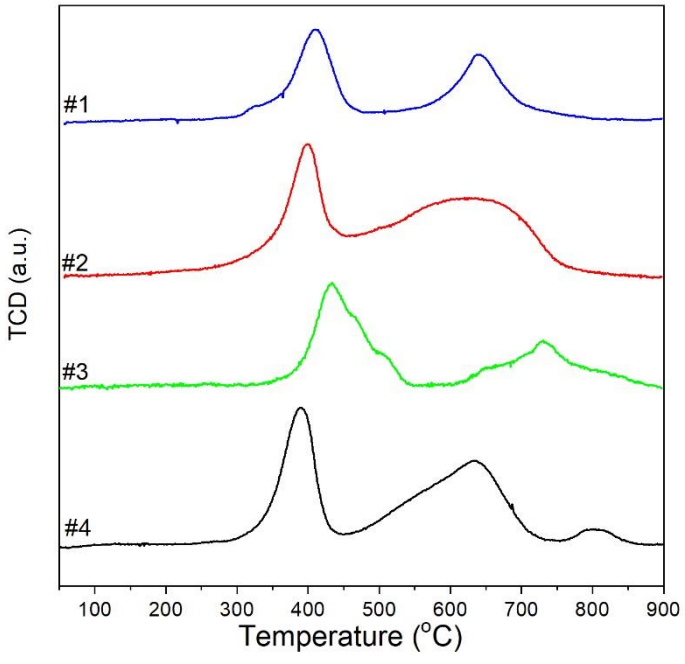

Figure 2 Temperature programmed reduction profiles of multimetal spinel oxides.

3.3 Reverse water gas shift catalytic experiments using multi-metal spinel oxides with MOF-programed compositions

Through the incorporation of multiple metal atoms in MOF SBUs, and their subsequent thermal transformation, we have now a batch of spinel oxide samples with adjustable amount of cobalt in their composition. Moreover, cobalt atoms might be at different crystallographic sites in the spinel structures, depending on the initial metal ratios. These differences are expected to impact the formation process of the active species under the RWGS selected reaction conditions, and thus result in different catalytic activity and selectivity. Figure 3(a) depicts the CO_2 conversion versus time on stream for catalyst derived from spinel oxides, in turn obtained from MOF samples, for the RWGS reaction at 700 °C, during 6 h. From the graphs it can be seen different trends and evolution of CO_2 conversion and CO selectivity among the different catalysts. A short induction period of around 2 h is observed in the case of the catalyst #1, obtained from MOF ZnMnCoCa 1441. After this time, the maximum conversion reached is 49%, with 100% of selectivity to CO (49.2% yield to CO). Similarly, catalyst #3 (ZnMnCoCa 1111) also shows an increase of conversion values with time, now reaching a conversion of 40% with a CO selectivity of 100% (39.7% yield to CO). On the other hand, catalyst #2, and #4, obtained from MOF samples MnCoCa122 and ZnMnCo118, respectively, do not show any induction period. Remarkably, a very high activity is already obtained after only 30 min of reaction time, reaching more than 55% conversion in both cases, and with nearly 100% selectivity to CO (54.6% and 53.9% yield to CO, for #2 and #4, respectively). It is worth noting that these values are near the ~ 60% thermodynamic equilibrium limit for the selected working conditions of H_2/CO_2 ratio and reaction temperature [3], ranking these catalysts among the most efficient ones for this reaction [3, 26–33] (Table S3 in the Electronic Supplementary Material (ESM)).

To further investigate the nature of the active species in these catalytic systems, we first PXRD measurements of the samples recovered after RWGS reaction. In all cases, the presence of metallic cobalt is clearly observed in the patterns (Fig. 4), as well as manganese oxide MnO. These two species are formed *in situ* under the reducing atmosphere used in the reaction. We also noticed that for those sample containing calcium, diffraction peaks corresponding to MnO are broader, and possibly split, suggesting that particles with slightly different lattice parameters are formed. Considering that no CaO is detected in the PXRD patterns, this can be attributable to inhomogeneous insertion of calcium atoms in the MnO structure.

Thus, metallic Co species appear as the catalytic active sites for RWGS. Indeed, a correlation between cobalt amount in the spinel oxides and resulting yield to CO is evidenced (Fig. 3(b)). Furthermore, at the view of the TPR profile catalysts #1, #2 and #4 exhibit a complete reduction at 700 °C, which is in line with the very good activity of these samples. On the other hand, the lower CO_2 conversion observed for the catalyst #3 is attributed to the lower reduction proportion due to the higher temperature required to produce metallic cobalt which is not complete until a temperature above 850 °C, which is higher than the reaction temperature. This also explains the greater induction period observed for this catalyst during the reaction. On the other hand, the increase in Mn species leads to a slight decrease in the CO selectivity, favoring the production of CH_4 [34], as it is evidenced in the MnCoCa 122 sample (#2 catalyst) (see Table S3 in the ESM).

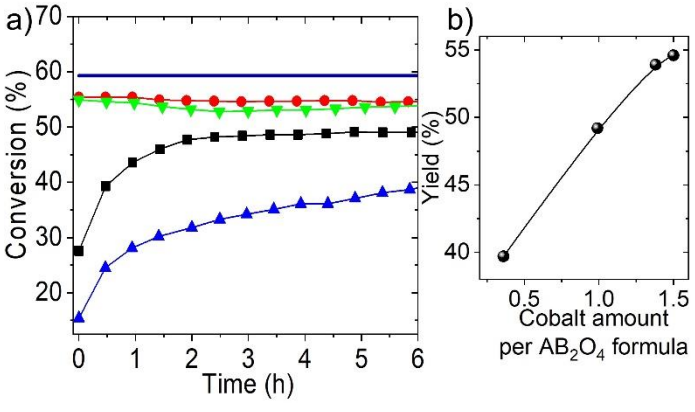

Figure 3 (a) CO_2 conversion versus time on stream at 700 °C and 0.1 MPa for ZnMnCoCa 1441(#1, black), MnCoCa 122 (#2, red), ZnMnCoCa 1111 (#3, blue), ZnMnCo 118 (#4, green) and maximum (thermodynamic equilibrium) conversion for this reaction conditions (dark blue). (b) Correlation between the CO yield of RGWS reaction vs. the amount of cobalt in the spinel pre-catalysts.

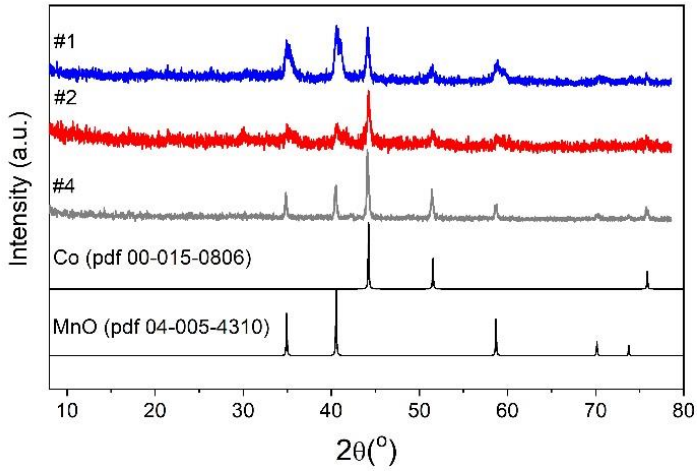

Figure 4 PXRD pattern of catalysts after reaction and their comparison with those corresponding to metallic Co and MnO.

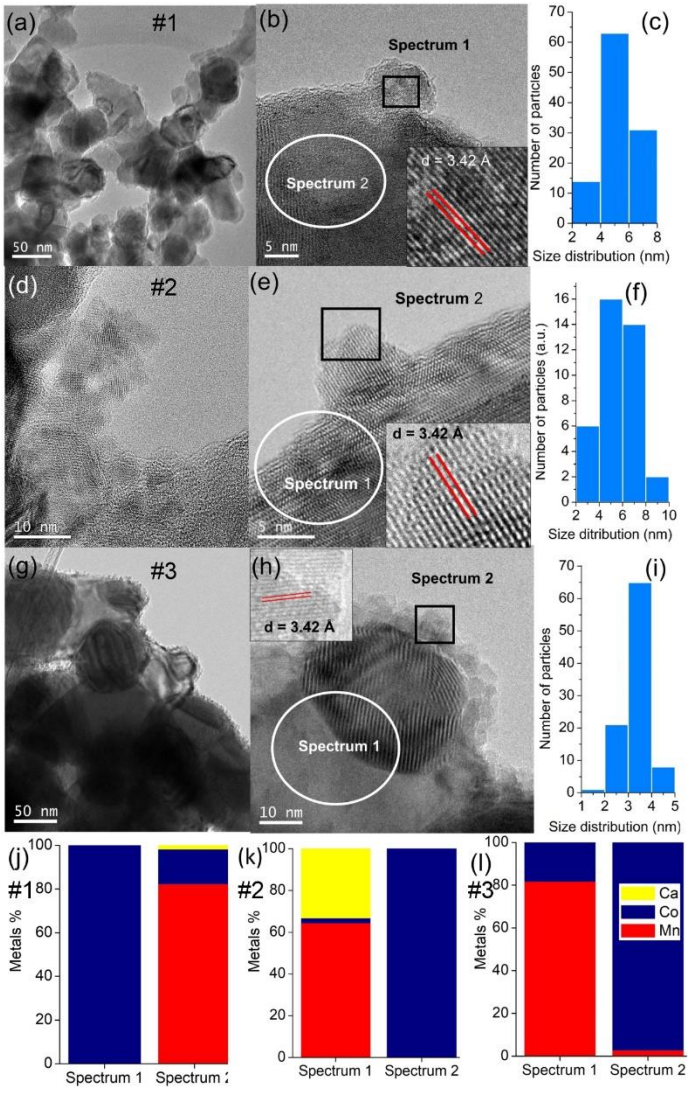

Figure 5 TEM-EDS study of catalyst after reaction, including #1 (first row), #2 (second row) and #4 (third row). (a), (d), and (g) TEM images of post-reaction materials; (b), (e), and (h) zoom of previous (a), (d), and (g) zones, respectively (inset images show the crystallographic (001) plane of metallic Co). (c), (f), and (i) Plots of the metallic cobalt particle size distribution. (j)–(l) The percentages of metal elements determined in the EDS spectra collected for the indicated areas.

TEM images evidences aggregates of two types of particles with different sizes (Fig. 5). According to EDS analysis, the large size particles, (> 50 nm) are mainly composed of manganese, corresponding to MnO as observed by PXRD. For catalysts #1 and #2, the presence of calcium is also detected in the same particles by EDS. This is consistent with the above explained PXRD analysis, which suggest the formation of a calcium doped MnO structure. However, we noticed that the Ca/Mn ratio differs between different particles (see the ESM). This is also consistent with the peak broadening and splitting in the PXRD patterns of the corresponding samples, since small changes in lattice parameters are expected for different degree of calcium substitution of the manganese sites in MnO. EDS analysis did not show any presence of zinc in the catalysts, indicating that any zinc species formed during the reaction are reduced and sublimated during the reaction [35, 36].

Ultra-small nanoparticles covering the surface of MnO are also observed, which correspond to metallic cobalt, as confirmed by EDS analysis. The size of these nanoparticles is quite homogeneous, with slight differences in each sample. Thus, for the catalyst #4, obtained from the ZnMnCo 118 MOF, most of these nanoparticles are in the 3.0–4.0 nm size range, while for catalysts #1 and #2 (ZnMnCoCa 1441 and MnCoCa 122, respectively), they are in the 4.0–8.0 nm range. This TEM study indicates that the catalytically active species are MnO-supported cobalt nanoparticles. The ultra-small size of the particles, and their distribution and accessibility on the surface of MnO are favoring the high activity of the catalysts due to high surface/volume ratio.

3.4 *In situ* experiments to define RWGS reaction pathways

To get insight in the structure–reactivity relationship a series of *in situ* experiments consisting of variable temperature powder X-ray diffraction, and NAP-XPS were performed with the sample #2 (MnCoCa122) to determine the structural, chemical and surface changes under reaction conditions.

In situ XRD experiments under H_2:CO_2 (2:1) atmosphere show how the spinel structure as determined by NPD $Mn_{0.69}Co_{1.50}Ca_{0.81}O_4$, is maintained until 400 °C. At this temperature, it starts to segregate CoO species (COD 1533087) with cubic structure and a cell parameter of a = 4.363 Å. The amount of cobalt oxide species progressively increases with the temperature. The detected broadening of these peaks indicates the presence of MnO (COD 1010393) also with cubic structure and cell parameter of a = 3.568 Å. Around 620 °C the presence of fcc cobalt (COD 1534891) is detected (cell parameter of a = 3.582 Å), which coexists with a $Mn_{1-x}Ca_xO$ phase (COD 1010393; a = 4.458 Å). These data are consistent with TPR studies above discussed.

Following, we performed an *in situ* NAP-XPS study of catalyst #2, (MnCoCa 122) under relevant reaction conditions in order to monitor the evolution of the surface chemistry of this sample as it reaches reaction conditions. The evolution of the spectral features as the sample is exposed to 2 mbar of a 2:1 H_2:CO_2 mixture and high temperature can be followed in Fig. 6. These experiments evidence differences in the surface reduction processes in comparison with bulk one. The spectrum of catalyst #2 in the Mn 2p, Mn 3s and Co 2p regions at room temperature consists of complex features of multiple splitting and satellites.

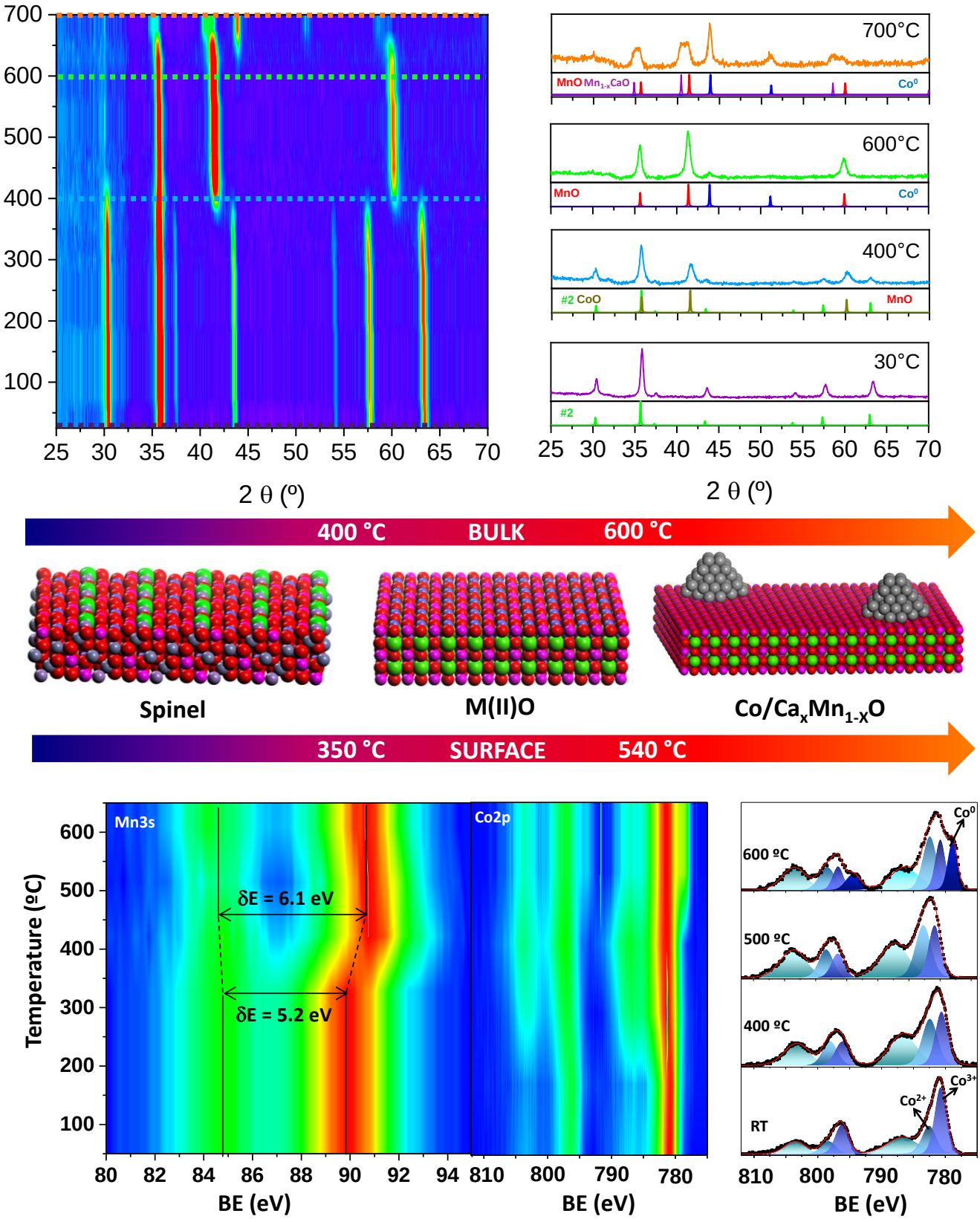

Figure 6 *In situ* characterization of catalyst #2 under reaction conditions. In the upper part, two-dimensional (2D) and selected variable temperature X-ray diffraction patterns with simulated crystal phase patterns: #2

structure (light green, obtained from Rietveld neutron powder refinements), CoO (dark green), MnO (red), $Mn_{1-x}Ca_xO$ (purple) and metallic cobalt (blue). In the bottom part: NAPXPS of Mn 3s and Co 2p signal and selected spectra at different temperatures. In the middle, illustration of bulk and surface differences in the crystal and chemistry properties during the formation of the active species, where M is Ca, Co, Mn, Zn. Color atoms: oxygen (red), cobalt (blue); zinc (light grey); manganese (magenta), calcium (green) and metallic cobalt (dark grey).

Spectral features in the Mn 2p region are characteristic of Mn(III) (with Mn $2p_{3/2}$ maximum at 642.1 eV), and so is the magnitude of the ca. 5.2 eV Mn 3s peak split (Fig. 6). Upon increasing the temperature to 400 °C, clear spectral satellites emerge in the Mn 2p region, which are characteristic of Mn(II). Together with an increase of the Mn 3s split from 5.2 to 6.1 eV, these spectral changes suggest that the reduction of Mn(III) to Mn(II) has occurred. The oxidation state of manganese ions was determined using the Galakhov et al. approach [37]. The splitting of the Mn 3s core-level spectrum originates from the exchange coupling between the Mn 3s hole and Mn 3d electrons. The magnitude of this splitting is proportional to (2S + 1), where S is the local spin of the 3d electrons in the ground state. Figure 6 shows the Mn 3s region for all temperatures. The Mn 3s split (δE) has been used to determine the average oxidation state of Mn at each temperature using the values provided by Alvarez Galvan et al. [38]. Thus, in this material the manganese valence is changing from $Mn^{3.1+}$ to $Mn^{2.1+}$. On the other hand, the Co 2p region contains two contributions: a first peak at 780.3 eV that can be ascribed to Co(III) in an octahedral environment, and a second peak at 782.6 eV, which can be assigned to Co(II) ions in a tetrahedral environment, characteristics of spinel structures [39, 40]. In addition, the presence of a satellite peak mainly attributed to the existence Co^{2+} states is also observed [41]. In the Co 2p region, the relative spectral intensity of feature associated with Co^{3+} decreases and the feature associated with Co^{2+} increases upon increasing the temperature from ca. 350 °C, in the reactive mixture of H_2 and CO_2. These observations suggest that Co(III) has been reduced to Co(II). Changes on the surface chemistry correlates well with results from *in-situ* XRD heat-treatment, where the structural bulk changes to CoO and MnO are detected for temperatures higher than 400 °C. The spectroscopic features remain stable upon further increasing the temperature up to 500 °C. However, a prominent low BE shoulder in the Co 2p region, associated with Co^0, emerges when the temperature reaches ca. 540 °C. Although the presence of metallic cobalt can only be observed at temperatures above 650 °C in the PXRD pattern, our NAP-XPS study shows surface metallic Co is formed at lower temperature. In accordance with the *in situ* XRD study, no further changes in Mn spectral features can be observed, indicating Mn species remains in the +2 oxidation state up to 600 °C under the reactive mixture.
The O 1s core level spectra for catalyst #2 in presence of a 2:1 H_2:CO_2 reactive mixture was also recorded from room temperature (RT) up to 600 °C. The O 1s spectra (Fig. 7(a)) at UHV can be fitted with three components located at 529.8 eV, assigned to lattice oxygen (O_x), 531.1 eV assigned to surface absorbed OH (O_{OH}), 532.7 eV assigned to surface carbon oxides (O_{C-Ox}). Upon introduction of the gas mixture, and as the temperature rises, the intensity of components assigned to O_{OH} and O_{C-Ox} groups increases relative to that of lattice oxygen (O_x), indicating that there is an accumulation of carbonyl, formate and carbonate species due to reaction intermediates and hydroxyl species probably also due to adsorbed water as reaction product [42]. These results are further confirmed by the examination of the changes observed in C 1s signal, which exhibit the following components in the pristine sample: 284.4 eV (C–C), 285.8 eV (C–OH), 287.8 eV (C=O), 289.1 eV (CO_3^{2-}). The introduction of reactive gases shows an increase in CO_3^{2-} and C–OH signals and the presence of a new band at 292.5 eV assigned to CO_2 in gas phase. Above 500 °C the increase of C=O and C–OH signals is more marked indicating the formation of reaction intermediates and the starting of formation of CO as product. Finally, at higher temperatures above 600 °C the CO_3^{2-}/HCO_3^- species increased and a new peak was observed at 282.0 eV, which is attributed to the carbidic carbon [43, 44] (Fig. 7(b)). At the view of these results, a plausible reaction pathway involves adsorption of CO_2 on the catalyst support surface, possibly favored by presence of calcium atoms and oxygen vacancies, as well dissociation of H_2 molecules promoted by metallic cobalt nanoparticles. This is followed by migration of hydrogen atoms and formation of intermediates, such as formate, carbonyl, and carbonate species, as detected in the XPS spectra. Finally, carbon monoxide and water are formed and released from the surface (Fig. 7(c)).

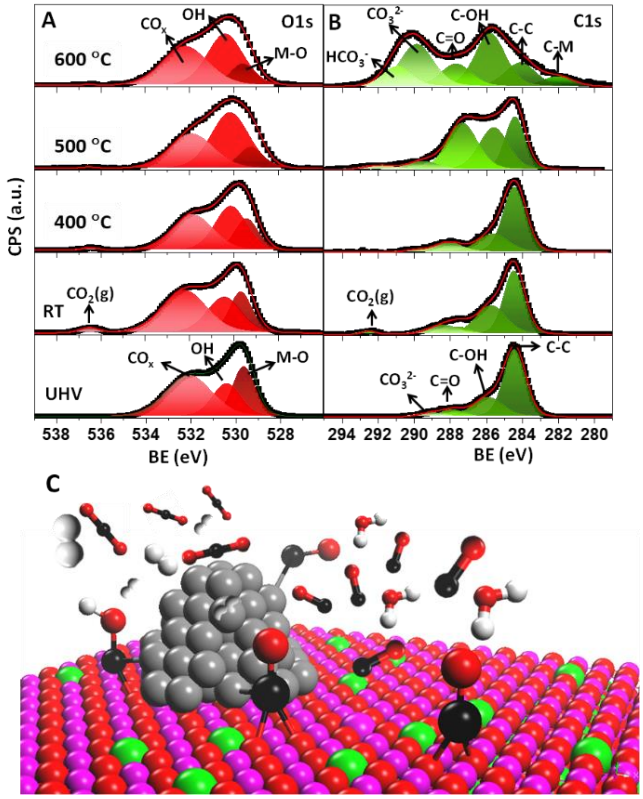

Figure 7. NAP XPS spectra of (A) O 1s and (B) C 1s signals. (C) Illustration of intermediate species found with use of #2 catalyst for reverse water gas shift reaction. Color atoms: oxygen (red); manganese (magenta), calcium (green), metallic cobalt (dark grey), carbon (black) and hydrogen (white).

Conclusions

Reticular chemistry allows the precise control of the metal composition of spinel oxides by the pre-arrangement of the desired metal elements in the SBU of a MOF, followed by a simple calcination process. Through this precise control of the metal atoms distribution, the reactivity of the resulting oxides is modified, in such a way that highly active and selective catalysts can be produced under selected catalytic conditions. Thus, the *in situ* formation of ultra-small metallic cobalt nanoparticles supported on manganese oxide is accomplished with the reduction of multimetal spine oxide as precursors. Through this route, it is possible to create catalysts with very high activity and selectivity for the reduction of carbon dioxide to carbon monoxide with hydrogen, reaching conversion values near the thermodynamic equilibrium under high space velocity, and 100% selectivity to carbon monoxide with certain compositions. This is among the most active and selective catalyst for the industrially and environmentally relevant reverse water-gas shift reaction.

Acknowledgements

We acknowledge Institut Laue-Langevin and Spanish initiatives on Neutron Scattering (ILL-SpINS) for beamtime at instrument D2B and G. Cuello for assistance during data acquisition (10.5291/ILL-DATA.5-21-1114). We thank M. C. Capel for the TEM images and TEM-EDS analysis acquisition at Instituto de Catálisis y Petroleoquímica (CSIC). Funding: Work at Instituto de Ciencia de Materiales de Madrid – Consejo Superior de Instigaciones Científicas (CSIC) has been supported by the Spanish Research Agency (Agencia Estatal de Investigación, AEI), Projects MAT2016-78465-R and CTQ2017-87262-R. This work was supported by the EU (ERC CoG HyMAP 648319) and Spanish MINECO (ENE2016-79608-C2-1-R). Authors also wish to thank to "Comunidad de Madrid" and European Structural Funds for their financial support to FotoArt-CM project (S2018/NMT-4367). F. G. acknowledges financial support from MINECO Ramón y Cajal program (RyC-2015-18384).

Electronic Supplementary Material: Supplementary material (additional experimental details, summary of

Rietveld refinement results, additional microscopy images and NAPS spectra) is available in the online version of this article at https://doi.org/10.1007/s12274-020-2813-x.

References

[1] Hepburn, C.; Adlen, E.; Beddington, J.; Carter, E. A.; Fuss, S.; Mac Dowell, N.; Minx, J. C.; Smith, P.; Williams, C. K. The Technological and Economic Prospects for CO_2 Utilization and Removal. *Nature* **2019**, *575* (7781), 87–97.

[2] de la Peña O'Shea, V.; Menéndez, N.; Tornero, J. D.; Fierro, J. L. G. Unusually High Selectivity to C2+ Alcohols on Bimetallic CoFe Catalysts During CO Hydrogenation. *Catal. Letters* **2003**, *88*, 123–128.

[3] Su, X.; Yang, X.; Zhao, B.; Huang, Y. Designing of Highly Selective and High-Temperature Endurable RWGS Heterogeneous Catalysts: Recent Advances and the Future Directions. *J. Energy Chem.* **2017**, *26* (5), 854–867.

[4] Daza, Y. A.; Kent, R. A.; Yung, M. M.; Kuhn, J. N. Carbon Dioxide Conversion by Reverse Water-Gas Shift Chemical Looping on Perovskite-Type Oxides. *Ind. Eng. Chem. Res.* **2014**, *53* (14), 5828–5837.

[5] Álvarez Galván, C.; Schumann, J.; Behrens, M.; Fierro, J. L. G.; Schlögl, R.; Frei, E. Reverse Water-Gas Shift Reaction at the Cu/ZnO Interface: Influence of the Cu/Zn Ratio on Structure-Activity Correlations. *Appl. Catal. B Environ.* **2016**, *195*, 104–111.

[6] Porosoff, M. D.; Yan, B.; Chen, J. G. Catalytic Reduction of CO_2 by H_2 for Synthesis of CO, Methanol and Hydrocarbons: Challenges and Opportunities. *Energy and Environmental Science*. 2016, pp 62–73.

[7] Schumann, J.; Eichelbaum, M.; Lunkenbein, T.; Thomas, N.; Álvarez Galván, M. C.; Schlögl, R.; Behrens, M. Promoting Strong Metal Support Interaction: Doping ZnO for Enhanced Activity of Cu/ZnO:M (M = Al, Ga, Mg) Catalysts. *ACS Catal.* **2015**, *5* (6), 3260–3270.

[8] Furukawa, H.; Cordova, K. E.; O'Keeffe, M.; Yaghi, O. M. The Chemistry and Applications of Metal-Organic Frameworks. *Science.* **2013**, *341* (6149), 1230444.

[9] Ding, M.; Flaig, R. W.; Jiang, H. L.; Yaghi, O. M. Carbon Capture and Conversion Using Metal-Organic Frameworks and MOF-Based Materials. *Chem. Soc. Rev.* **2019**, *48* (10), 2783–2828.

[10] Boyd, P. G.; Chidambaram, A.; García-Díez, E.; Ireland, C. P.; Daff, T. D.; Bounds, R.; Gładysiak, A.; Schouwink, P.; Moosavi, S. M.; Maroto-Valer, M. M.; et al. Data-Driven Design of Metal–Organic Frameworks for Wet Flue Gas CO_2 Capture. *Nature* **2019**, *576* (7786), 253–256.

[11] Diercks, C. S.; Liu, Y.; Cordova, K. E.; Yaghi, O. M. The Role of Reticular Chemistry in the Design of CO_2 Reduction Catalysts. *Nat. Mater.* **2018**, *17* (4), 301–307.

[12] Nguyen, P. T. K.; Nguyen, H. T. D.; Nguyen, H. N.; Trickett, C. A.; Ton, Q. T.; Gutiérrez-Puebla, E.; Monge, M. A.; Cordova, K. E.; Gándara, F. New Metal-Organic Frameworks for Chemical Fixation of CO_2. *ACS Appl. Mater. Interfaces* **2018**, *10* (1), 733–744.

[13] Dang, S.; Zhu, Q.-L.; Xu, Q. Nanomaterials Derived from Metal–Organic Frameworks. *Nat. Rev. Mater.* **2018**, *3* (1), 17075.

[14] Zhang, E.; Wang, T.; Yu, K.; Liu, J.; Chen, W.; Li, A.; Rong, H.; Lin, R.; Ji, S.; Zheng, X.; et al. Bismuth Single Atoms Resulting from Transformation of Metal-Organic Frameworks and Their Use as Electrocatalysts for CO_2 Reduction. *J. Am. Chem. Soc.* **2019**, *141* (42), 16569–16573.

[15] Wu, Y.; Huang, Z.; Jiang, H.; Wang, C.; Zhou, Y.; Shen, W.; Xu, H.; Deng, H. Facile Synthesis of Uniform Metal Carbide Nanoparticles from Metal-Organic Frameworks by Laser Metallurgy. *ACS Appl. Mater. Interfaces* **2019**, *11* (47), 44573–44581.

[16] Jiang, H.; Jin, S.; Wang, C.; Ma, R.; Song, Y.; Gao, M.; Liu, X.; Shen, A.; Cheng, G. J.; Deng, H. Nanoscale Laser Metallurgy and Patterning in Air Using MOFs. *J. Am. Chem. Soc.* **2019**, *141* (13), 5481–5489.

[17] Castillo-Blas, C.; de la Peña-O'Shea, V. A.; Puente-Orench, I.; de Paz, J. R.; Sáez-Puche, R.; Gutiérrez-Puebla, E.; Gándara, F.; Monge, Á. Addressed Realization of Multication Complex Arrangements in Metal-Organic Frameworks. *Sci. Adv.* **2017**, *3* (7), e1700773.

[18] Castillo-Blas, C.; López-Salas, N.; Gutiérrez, M. C. C. M. C.; Puente-Orench, I.; Gutiérrez-Puebla, E.; Ferrer, M. L. L.; Monge, M. Á. Á.; Gándara, F. Encoding Metal-Cation Arrangements in Metal-Organic Frameworks for Programming the Composition of Electrocatalytically Active Multimetal Oxides. *J. Am. Chem. Soc.* **2019**, *141* (4), 1766–1774.

[19] Peng, L. M.; Cowley, J. M. EELS Analysis of Surface-Channelled Electrons. *Surf. Sci.* **1988**, *204* (3), 555–567.

[20] Abràmoff, M. D.; Magalhães, P. J.; Ram, S. J. Image Processing with ImageJ. In *Biophotonics International*; 2004; Vol. 11, pp 36–41.

[21] Häglund, J.; Fernández Guillermet, A.; Grimvall, G.; Körling, M. Theory of Bonding in Transition-Metal Carbides and Nitrides. *Phys. Rev. B* **1993**, *48* (16), 11685–11691.

[22] Radler, M. J.; Cohen, J. B.; Sykora, G. P.; Mason, T.; Ellis, D. E.; Faber, J. The Defect Structures of $Mn_{1-x}O$. *J. Phys. Chem. Solids* **1992**, *53* (1), 141–154.

[23] Richard, D.; Ferrand, M.; Kearley, G. J. Analysis and Visualisation of Neutron-Scattering Data. *J. Neutron Res.* **1996**, *4* (1–4), 33–39.

[24] Accelrys Inc. BIOVIA Materials Studio. *Http://Accelrys.Com/*materials-studio

[25] Bulavchenko, O. A.; Gerasimov, E. Y.; Afonasenko, T. N. Reduction of Double Manganese–Cobalt Oxides: In Situ XRD and TPR Study. *Dalt. Trans.* **2018**, *47* (47), 17153–17159.

[26] Wang, L.; Liu, H.; Chen, Y.; Yang, S. Reverse Water–Gas Shift Reaction over Co-Precipitated Co–CeO_2 Catalysts: Effect of Co Content on Selectivity and Carbon Formation. *Int. J. Hydrogen Energy* **2017**, *42* (6), 3682–3689.

[27] Dai, B.; Zhou, G.; Ge, S.; Xie, H.; Jiao, Z.; Zhang, G.; Xiong, K. CO_2 Reverse Water-Gas Shift Reaction on Mesoporous M-CeO2 Catalysts. *Can. J. Chem. Eng.* **2017**, *95* (4), 634–642.

[28] Aitbekova, A.; Goodman, E. D.; Wu, L.; Boubnov, A.; Hoffman, A. S.; Genc, A.; Cheng, H.; Casalena, L.; Bare, S. R.; Cargnello, M. Engineering of Ruthenium–Iron Oxide Colloidal Heterostructures: Improved Yields in CO_2 Hydrogenation to Hydrocarbons. *Angew. Chemie - Int. Ed.* **2019**, *58* (48), 17451–17457.

[29] Okemoto, A.; Harada, M. R.; Ishizaka, T.; Hiyoshi, N.; Sato, K. Catalytic Performance of MoO_3/FAU Zeolite Catalysts Modified by Cu for Reverse Water Gas Shift Reaction. *Appl. Catal. A Gen.* **2020**, *592*, 117415.

[30] Gao, P.; Li, S.; Bu, X.; Dang, S.; Liu, Z.; Wang, H.; Zhong, L.; Qiu, M.; Yang, C.; Cai, J.; et al. Direct Conversion of CO_2 into Liquid Fuels with High Selectivity over a Bifunctional Catalyst. *Nat. Chem.* **2017**, *9* (10), 1019–1024.

[31] Xu, H.; Li, Y.; Luo, X.; Xu, Z.; Ge, J. Monodispersed Gold Nanoparticles Supported on a Zirconium-Based Porous Metal-Organic Framework and Their High Catalytic Ability for the Reverse Water-Gas Shift Reaction. *Chem. Commun.* **2017**, *53* (56), 7953–7956.

[32] Wang, C.; Guan, E.; Wang, L.; Chu, X.; Wu, Z.; Zhang, J.; Yang, Z.; Jiang, Y.; Zhang, L.; Meng, X.; et al. Product Selectivity Controlled by Nanoporous Environments in Zeolite Crystals Enveloping Rhodium Nanoparticle Catalysts for CO_2 Hydrogenation. *J. Am. Chem. Soc.* **2019**, *141* (21), 8482–8488.

[33] Han, Y.; Xu, H.; Su, Y.; Xu, Z. liang; Wang, K.; Wang, W. Noble Metal (Pt, Au@Pd) Nanoparticles Supported on Metal Organic Framework (MOF-74) Nanoshuttles as High-Selectivity CO_2 Conversion Catalysts. *J. Catal.* **2019**, *370*, 70–78.

[34] Vrijburg, W. L.; Moioli, E.; Chen, W.; Zhang, M.; Terlingen, B. J. P.; Zijlstra, B.; Filot, I. A. W.; Züttel, A.; Pidko, E. A.; Hensen, E. J. M. Efficient Base-Metal NiMn/TiO2 Catalyst for CO_2 Methanation. *ACS Catal.* **2019**, *9* (9), 7823–7839.

[35] Junca, E.; de Oliveira, J. R.; Restivo, T. A. G.; Espinosa, D. C. R.; Tenório, J. A. S. Synthetic Zinc Ferrite Reduction by Means of Mixtures Containing Hydrogen and Carbon Monoxide. *J. Therm. Anal. Calorim.* **2016**, *123* (1), 631–641.

[36] de Siqueira, R. N. C.; de Albuquerque Brocchi, E.; de Oliveira, P. F.; Motta, M. S. Hydrogen Reduction of Zinc and Iron Oxides Containing Mixtures. *Metall. Mater. Trans. B* **2014**, *45* (1), 66–75.

[37] Galakhov, V. R.; Demeter, M.; Bartkowski, S.; Neumann, M.; Ovechkina, N. A.; Kurmaev, E. Z.; Lobachevskaya, N. I.; Mukovskii, Y. M.; Mitchell, J.; Ederer, D. L. Mn 3s Exchange Splitting in Mixed-Valence Manganites. *Phys. Rev. B* **2002**, *65* (11), 113102.

[38] Álvarez-Galván, M. C.; de la Peña O'Shea, V. A.; Arzamendi, G.; Pawelec, B.; Gandía, L. M.; Fierro, J. L. G. Methyl Ethyl Ketone Combustion over La-Transition Metal (Cr, Co, Ni, Mn) Perovskites. *Appl. Catal. B Environ.* **2009**, *92* (3), 445–453.

[39] Xu, L.; Jiang, Q.; Xiao, Z.; Li, X.; Huo, J.; Wang, S.; Dai, L. Plasma-Engraved Co3O4 Nanosheets with Oxygen Vacancies and High Surface Area for the Oxygen Evolution Reaction. *Angew. Chemie Int. Ed.* **2016**, *55* (17), 5277–5281.

[40] de la Peña O'Shea, V. A.; Álvarez-Galván, M. C.; Campos-Martin, J. M.; Menéndez, N. N.; Tornero, J. D.; Fierro, J. L. G. Surface and Structural Features of Co-Fe Oxide Nanoparticles Deposited on a Silica Substrate. *Eur. J. Inorg. Chem.* **2006**, *2006* (24), 5057–5068.

[41] Vaz, C. A. F.; Prabhakaran, D.; Altman, E. I.; Henrich, V. E. Experimental Study of the Interfacial Cobalt Oxide in Co3O4/AAl2O3 (0001) Epitaxial Films. *Phys. Rev. B* **2009**, *80* (15), 155457.

[42] Wang, W.; Wang, S.; Ma, X.; Gong, J. Recent Advances in Catalytic Hydrogenation of Carbon Dioxide. *Chem. Soc. Rev.* **2011**, *40* (7), 3703–3727.

[43] Jin, Y.; Sun, G.; Wang, Z.; Pan, H.; Xu, L.; Xu, H.; Huang, W. Elementary Surface Reactions on Co(0001) under Fischer–Tropsch Synthesis Conditions. *J. Phys. Chem. C* **2017**, *121* (39), 21535–21540.

[44] Beitel, G. A.; de Groot, C. P. M.; Oosterbeek, H.; Wilson, J. H. A Combined In-Situ PM-RAIRS and Kinetic Study of Single-Crystal Cobalt Catalysts under Synthesis Gas at Pressures up to 300 Mbar. *J. Phys. Chem. B* **1997**, *101* (20), 4035–4043.